Modeling, evaluation, and optimization of a self-bearing spinfilter for bioseparations

Journal Article

Author(s):
Beglinger, Lars; Steinert, Daniel; Nussbaumer, Thomas; Biela, Jürgen

Publication date:
2025-07-19

Permanent link:
https://doi.org/https://doi.org/10.3929/ethz-b-000716113

Originally published in:
Separation and Purification Technology 361, https://doi.org/10.1016/j.seppur.2024.131086

Separation and Purification Technology 361 (2025) 131086

Contents lists available at ScienceDirect

Separation and Purification Technology

journal homepage: www.elsevier.com/locate/seppur

Modeling, evaluation, and optimization of a self-bearing spinfilter for bioseparations

Lars Beglinger [a,*], Daniel Steinert [b], Thomas Nussbaumer [b], Jürgen Biela [a]

[a] ETH Zürich, Laboratory for High Power Electronics Systems, Physikstrasse 3, 8092 Zürich, Switzerland
[b] Levitronix GmbH, Bändliweg 30, 8048 Zürich, Switzerland

ARTICLE INFO

Communicated by Raquel Aires Barros

Keywords:
Bioseparations
Hydrodynamics
Microfiltration
Flux modeling
Spinfilter

ABSTRACT

Rotating filters promise many advantages for long-term separation processes of complex media such as cell cultures, but have never been commercialized on a large scale due to practical challenges and limited scalability. A bearingless spinfilter circumvents many of the drawbacks, yet additional considerations must be taken into account. Thus, an existing particle-force based model for cross-flow filtration, dependent on the membrane shear rate and the transmembrane pressure, is adapted to the spinfilter and predicts the behavior of retained particles at the membrane. Computational fluid dynamics simulations allow to calculate the shear rate at the membrane for the model. Additionally, with the simulated distribution of the shear rate and the energy dissipation rate within the spinfilter, a prediction of the hydrodynamic stress on cell cultures can be made. The model is verified with a spinfilter prototype on a yeast cell culture and is in good agreement with experimental results. Additional separation experiments with bovine blood serve to indicate the extent of cell damage induced by hydrodynamic stress within the spinfilter. The results demonstrate that operating the spinfilter at the optimum operation point leads to a faster separation process at a lower level of cell damage per volume of filtrate in comparison to a passive tangential flow filtration in hollow fibers.

1. Introduction

Rotating filter membranes were the research focus of several groups around the turn of the millennium. Concept descriptions and practical considerations [1,2], experimental investigations [3,4], and fluid simulations [5,6] have been intensively examined. The concept of non-stationary filter membranes promises very high shear rates on the membrane surface, which can efficiently remove retained particles by hydrodynamic forces in microfiltration. The required shear rate is generated directly on the membrane, thereby decoupling it from the retentate flow. In contrast, in passive tangential flow filtration (TFF) modules, the retentate flow serves as the primary source of the generated shear rate. Consequently, high retentate flow leads to a pressure gradient over the length of the passive TFF membrane, such as hollow fiber (HF) filters. This leads to non-uniform loading of the membrane and reduces the filtration performance.

Despite some commercial applications of rotating membranes for blood plasma filtration [7], laboratory analytical devices [8], and the paper industry [9], the concept of rotating membranes has not gained widespread adoption. One of the reasons for this is the increased design complexity of such filter modules, as well as the more complicated operation and more expensive maintenance due to the moving parts. Additionally, the rotating seals, from the drive to the submerged shaft of the filter module, represent a potential point of contamination and leakage. This renders them unsuitable for applications in high-purity environments, including those in semiconductor, pharmaceutical, and biotechnology industries. Furthermore, the scalability and packing density of rotating membranes is significantly lower than that of other filter modules [10]. For these reasons, among others, the investigation and use of rotating filter membranes has declined within the research community and separation industry, at least temporarily.

Nevertheless, the current trend in biotechnology suggests a transition from batch processing to continuous operation, or perfusion [11]. In continuous operation, the use of smaller vessels reduces the footprint and costs of the production plant by as much as 55% [12]. Moreover, it has been demonstrated that the quality of the proteins and monoclonal antibodies produced is superior due to the constant standing times [13]. Perfusion also allows for higher cell concentrations in the bioreactor than in batch processes [14]. It is widely accepted that non-stationary membranes have the capacity to filter higher particle concentrations than the currently utilized filter systems [10], such as hollow fiber or flat plate modules. Furthermore, in novel therapeutic modalities of precision medicine, therapeutic proteins are frequently produced in limited

* Corresponding author.
E-mail address: beglinger@hpe.ee.ethz.ch (L. Beglinger).

https://doi.org/10.1016/j.seppur.2024.131086
Received 17 October 2024; Received in revised form 9 December 2024; Accepted 13 December 2024
Available online 7 January 2025

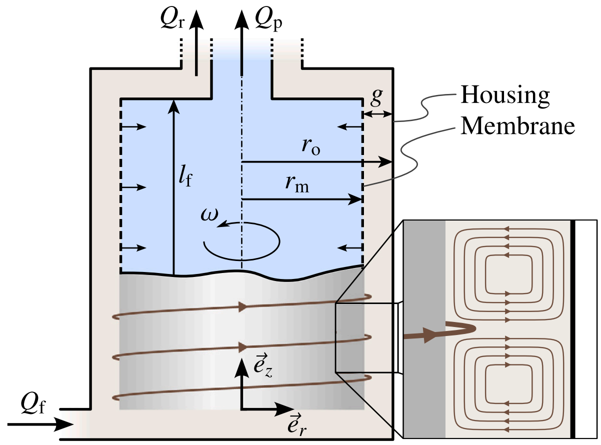

Fig. 1. The base geometry and relevant dimensions of a Taylor–Couette cell are presented in a schematic view. In the rotating annular gap, high wall shear rates γ_m are generated due to the collapsing streamlines resulting in Taylor vortices once the inertial forces in the fluid dominate the viscous forces. A pair of counter-rotating Taylor vortices is shown in the inset.

quantities for individual patients [15–17], where the disadvantage of scalability is rendered less significant.

In the case of shear-sensitive cell cultures, it is essential to maintain the hydrodynamic stress caused by the shear rate for cross flow filtration at a minimum while ensuring that a certain level of shear drag on the retained cells is still present to enable cross-flow filtration. Ideally, this occurs directly on the membrane only. In passive TFF, the entire fluid is pumped through the filter module at a high retentate flow in order to generate the necessary shear rate. This results in elevated shear rates not only within the filter module but also within the pump, the tubing, and other components of the fluid circuit. It is therefore to be expected that significant cell damage occurs, depending on the specific process and cell culture in question.

In the meantime, since rotating membrane filters have been replaced by more scalable filter systems in research and industry, bearingless motors in centrifugal pumps and other applications for contactless drives in hermetically sealed housings have become a mature technology in industries with very high demands on cleanliness and reliability, such as semiconductor and pharmaceutical industries [18,19]. The magnetic levitation of the rotor enables contactless operation of the moving parts, thereby circumventing the need for rotating seals to the external environment [20]. Similar to pumps, the adoption of this technology to a spinfilter allows for the elimination of many of the disadvantages associated with traditional rotating filters, while simultaneously exploiting their numerous advantages, particularly for perfusion in biotechnology applications.

The proof of concept of a bearingless spinfilter has been presented in [21]. In [22], potential topologies were investigated to prevent the remixing of the feed with the filtrate through an unavoidable internal gap between the feed and filtrate, despite the prevailing transmembrane pressure (TMP). An integrated impeller on the spinfilter rotor generates the TMP directly within the filter module, as seen in the schematic in Fig. 1. Therefore, both the TMP and the shear rate on the membrane scale with the rotational speed. The ratio of the membrane and impeller radii determines the TMP and is locked for each prototype.

In this publication, the optimal operation point of a bearingless spinfilter in terms of the TMP and the shear rate on the membrane is determined. In Section 2, an existing cross-flow microfiltration particle-force based model is adapted to the bearingless spinfilter and predicts the detachment of retained particles from the membrane, and thus, the filter flux. With computational fluid dynamics (CFD) simulations in the annular gap, a new empirical formula for the shear rate on the membrane, dependent on the rotational speed and the annular gap width, is derived. Finally, the energy dissipation rate (EDR) of the spinfilter is addressed, which gives insight into the cell viability during operation and allows for a comparison with similar research.

For validating the adapted particle force model, a new prototype, presented in Section 3, employs an internal lip seal between the feed and filtrate, which allows to set the TMP and the membrane shear rate independently. Additionally, the experimental methods are discussed, including tests of the spinfilter prototype and reference filter modules to separate a yeast cell culture from water. Furthermore, the hemolysis rate is measured during bovine blood filtration and serves as an indicator of the degree of cell damage under various operation conditions. The results of these experiments are presented and discussed in Section 4 and contextualized for the application of a bearingless spinfilter in biotechnology in Section 5.

2. Theoretical background

The phenomena of membrane fouling and cake formation are complex phenomena, and thus are modeled, approximated, and attempted to be understood using a variety of approaches in order to predict the filtrate flux more accurately and design separation processes more efficiently. Among the approaches employed are mass transfer models [23], surface energy theory [24], and combined pore blocking models [25]. While the various theories align well with laboratory measurements under isolated conditions, the majority of researchers highlight that real fluids and complex suspensions remain poorly understood. Especially in biotechnology applications, the process fluid comprises a range of complex components, including chemically diverse nutrient media, secreted organic substances such as proteins and antibodies, and cell fragments from destroyed cells, in addition to the cell culture itself.

2.1. General particle force model

A straightforward approach for robust and precise particle deposition predictions regarding experiments, particularly for microfiltration, is a particle-force based model. Thereby, the forces acting on a single, spherical particle within the fluid are modeled. Due to the TMP, the retained particle is pressed against the membrane. Two distinct methods for calculating the filtration force F_{TMP} are employed in literature: One approach is to assume that the TMP acts on the area of the pore opening according to [26]

$$F_{\mathrm{TMP}} = A_{\mathrm{pore}} \cdot \mathrm{TMP} = \frac{\pi d_{\mathrm{pore}}^2}{4} \cdot \mathrm{TMP}, \tag{1}$$

with the pore diameter d_{pore} and the transmembrane pressure TMP. In most microfiltration applications, both parameters are known, making this method straight-forward to calculate. In the case of high particle concentrations, particle–particle interactions result in a deviation of Eq. (1), as the particles block each other, and thus no longer fully adhere to the membrane surface and its pores. Alternatively, the filtration force F_{filt} is calculated as a drag force, given by

$$F_{\mathrm{filt}} = 3\pi\, \eta\, d_{\mathrm{p}}\, v_{\mathrm{filt}}, \tag{2}$$

with the dynamic viscosity of the suspension η, the particle diameter d_{p}, and the filtration flow velocity v_{filt} [27]. The second approach requires measurement data, as the filtration flow velocity v_{filt} cannot be predicted precisely without exactly knowing the porosity, structure, and even the chemical composition and surface modifications of the membrane, which all might influence the membrane flux. In this publication, TMP-based approach in Eq. (1) is used due to its simplicity.

Meanwhile, the drag force due to the relative motion of the fluid with respect to the membrane acts in parallel to the membrane surface, dragging the particles along the surface and detaching them. In the micrometer vicinity of the membrane, the velocity field can be linearized, whereby the shear rate on the membrane γ_m serves to determine the gradient of the approximated flow profile. The shear drag force F_γ is given by

$$F_\gamma = 3\pi\,\eta\,d_\mathrm{p}^2\,\gamma_\mathrm{m}, \tag{3}$$

with the shear rate γ_m. It should be noted that the quadratic scaling of the particle size d_p compared to the linear dependency in Eq. (2) originates from averaging the velocity of the flow field over the particle diameter. A comprehensive derivation of the shear rate for the spinfilter and the reference TFF module is presented in Section 2.3.

Furthermore, the non-uniform velocity profile on a particle induces a lift force. Nevertheless, the numerical value of the lift force in a realistic range of shear rates is insignificant and can be disregarded [28]. Similarly, the centrifugal force exerted on a particle due to rotation can be neglected. In contrast to the other surface-based forces, which scale quadratically with particle (or pore) size, the particle mass-based centrifugal force increases with the cube of the particle size. In the typical micrometer size range for cells, this results in a coefficient of the centrifugal force that is approximately 100 000 times smaller than the surface-based drag or filtration forces.

In [28], the two main forces are geometrically related around a center of rotation with a torque detachment condition. This approach requires perfectly round pores and spherical particles, which are not realistic assumptions for complex biological suspensions.

In [26], however, the author applies a static friction coefficient λ_fr to relate the orthogonal forces and defines the detachment criterion as

$$F_\gamma > \lambda_\mathrm{fr} F_\mathrm{TMP} \tag{4}$$

for which the value of λ_fr is then empirically determined by measurements. The physically unrealistically high values for λ_fr suggest that additional, surface energy interactions, such as van der Waals forces, play a significant role. However, in the overall particle force model, this effect merely leads to an offset of the orthogonal filtration force F_TMP. For this work, and the considered cell suspensions, the force relation with a static friction coefficient is expected to yield more robust predictions with respect to the particle detachment state, and thus, the membrane flux. To conclude, out of the different approaches, Eqs. (1) and (3) are used in Eq. (4). The permeate flow drag force approach serves as a backup in case the model agreement with the measurement data is insufficient and other dependencies are required to be integrated in the model.

2.2. Spinfilter particle force model

The particle force model must be adapted for the spinfilter in a number of ways. The version specific to the spinfilter with all relevant forces is depicted in Fig. 2**(a)** First, the TMP is reduced by the rotational speed due to the internal centrifugal pressure of the filtrate and the pressure distribution in the annular gap. The resulting TMP of the superimposed effects is given by

$$\mathrm{TMP} = p_\mathrm{ext} - c\omega^2 \tag{5}$$

where p_ext is the externally applied (vacuum) pressure and c is an empirical coefficient for the chosen annular gap geometry. With Eq. (5), the perpendicular force exerted on the particle towards the membrane is then given in Eq. (1). Furthermore, a constant force F_charge is introduced to represent the adhesion forces and surface energy interactions between the retained particles and the membrane surface. The total particle-attaching force is given by

$$F_\mathrm{fr} = \lambda_\mathrm{fr}(F_\mathrm{TMP} + F_\mathrm{charge}) \tag{6}$$

where the static friction coefficient method described in Section 2.1 is used due to reasons of increased robustness. F_charge is determined by measurements.

The lateral drag force F_γ due to the shear rate is directly obtained from Eq. (3), where γ_m is determined by the CFD simulations in Eq. (9) for the selected spinfilter geometry with membrane radius $r_\mathrm{m} = 15.5$ mm

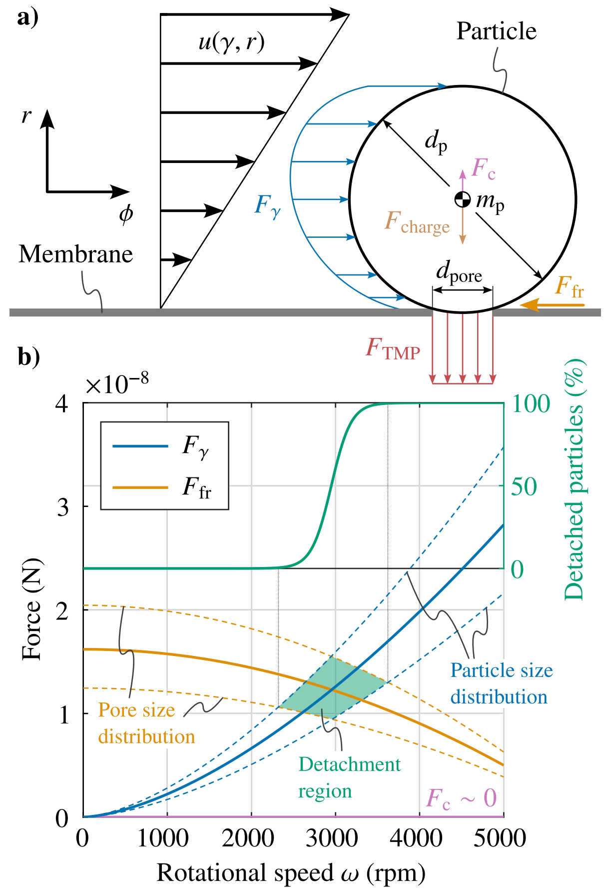

Fig. 2. A particle force based modeling approach for the spinfilter in microfiltration captures the hydrodynamic effects on retained particles with respect to the shear rate γ_m on the membrane. **(a)** A retained particle on the filter membrane is subjected to different forces, where the filtration force F_TMP due to the transmembrane pressure (TMP) and the parallel shear drag force F_γ play the most important roles. The orthogonal forces are related to each other with a friction coefficient λ_fr, from which the friction force Ffr is concluded. **(b)** The forces of opposite directions in parallel to the membrane, F_γ and F_fr, are shown over the rotational speed range ω for a constant external pressure difference $p_\mathrm{ext} = 0.7$ bar. Due to the particle size distribution $d_\mathrm{p} = \mathcal{N}(\mu_\mathrm{p} = 6.1\,\mu\mathrm{m}, \sigma_\mathrm{p} = \pm 0.3\,\mu\mathrm{m})$, and pore size distribution $d_\mathrm{pore} = \mathcal{N}(\mu_\mathrm{pore} = 0.8\,\mu\mathrm{m}, \sigma_\mathrm{pore} = \pm 0.05\,\mu\mathrm{m})$, instead of a singular detachment point, there exists a detachment region with a cumulative detachment probability. The percentage of detached particles is modeled as a sigmoid function with a varying slope steepness, depending on the width of the size distributions.

and annular gap width $g = 1.5$ mm. Finally, the detachment criterion is formulated as $F_\gamma > F_\mathrm{fr}$ to remove a particle from the membrane surface.

Fig. 2**(b)** presents an operation point, where the reduction of the TMP is reflected in the reduction of F_fr with increasing rotational speed ω. Meanwhile, the shear drag force F_γ increases for faster rotational speeds until the parallel force equilibrium is reached. However, the superimposed particle and pore size distributions attenuate the impact of the particle detachment criterion with a cumulative probability function. Instead of an operation point where the particle detachment acts as a step function, a progressive particle detachment is expected. The width of the size distribution of the pores and particles dictates the slope steepness of the resulting sigmoid curve.

In cases where there are significant deviations from a Gaussian fit, for instance, due to the presence of multiple solid components within a complex suspension, the size distribution could be represented in a discrete manner. This approach results in the generation of activation functions specific to the suspension in question. However, in order to maintain the model's simplicity, a standard sigmoid function is

Table 1
Three scalar parameters are fitted to the measurement data. The base porosity is indicated for the 0.8 μm membrane, for which the measurement data is the most robust.

Parameter	Fit value	Unit
F_{charge}	1.1×10^{-9}	N
Sigmoid flank	4.3×10^{7}	[–]
Base porosity (0.8 μm)	1.47×10^{-16}	m^2

assumed here, with the steepness of the slope being an adjustable, scalar parameter retrospectively fitted by measurement results.

A higher shear rate at the membrane allows for a higher TMP without significant particle deposition, thereby facilitating a higher filtrate flow. The membrane flux is calculated in accordance with Darcy's law, whereby the cumulative particle detachment probably affects the base porosity of the membrane. The base porosity represents a third open scalar within the particle force model, which allows for a comparison of the particle force model with measurement data. All three fitted parameters with respect to the measurements are shown in Table 1.

2.3. Shear rate on the rotating cylinder wall

The shear rate γ_m is the critical parameter for the detachment of particles from the membrane in the particle force model. Therefore, its exact determination for the rotating filter membrane in the annular gap is of great importance. Taylor [29] derives the flow behavior in the rotating annular gap between two concentric cylinders from the Navier–Stokes equations and extends the dimensionless Reynolds number according to the geometry and formulates the Taylor Number

$$Ta = \frac{\omega r_m^{1/2} g^{3/2}}{\nu} \tag{7}$$

where ω denotes the rotational speed of the inner cylinder, r_m is the radius of the inner cylinder, or the radius of the membrane, respectively, g is the annular gap, and ν the kinematic viscosity of the fluid. When the inertial fluid forces dominate the viscous forces at $Ta > 42$, the Couette stream lines collapse and form regularly spaced Taylor vortices. Thus, an axial shear component is superpositioned to the Couette shear on the membrane. Taylor derives the shear rate on the inner rotating cylinder in an annular gap

$$\gamma_m = 0.23\ \omega^{3/2}\ r_m^{5/4}\ g^{-1/4}\ \nu^{-1/2}, \tag{8}$$

which is valid for $60 < Ta < 3000$. The necessary assumptions to analytically solve the differential equations assumes $r_m \gg g$ with an infinitely small gap g. However, for realistic gap dimensions, some deviation and loss of accurate predictions must be expected.

With computational fluid dynamics (CFD) simulations, a more precise shear rate γ_m on the membrane surface in the annular gap is calculated as a function of the rotational speed and the annular gap width for a set inner radius r_m for this research, when the real geometry deviates too much compared to Taylor's assumptions. Two-dimensional axisymmetric simulations of the annular gap are an efficient computational approach. To mitigate the impact of axial boundary conditions, only the central region without any disturbances by the domain boundaries is evaluated. Since the Taylor Number $Ta > 400$ at the operational range limit of the rotational speed $\omega = 5000\,\text{rpm}$, fully turbulent flow is expected under some of the simulated conditions. Thus, the k-omega SST turbulence model [30] is employed as it is known to yield the most accurate results for wall-confined flows. The investigated region and the flow field of an operating example at one operating point are illustrated in Fig. 3**(a)**, which confirms the formation of Taylor vortices. The flow instabilities locally enhance the shear rate on the membrane as seen in the progression of the element-wise shear rate $\gamma_{m,el}$ over the length of the rotating membrane. Due to the superimposed axial through-flow in the spinfilter, the flow instabilities propagate in a spiral-like shape through the annulus. This means that every part of the membrane periodically experiences the maximum shear rate multiple times per second even for small axial through-flows. Since particles are transported to and deposited by the separation process on the membrane over time, but can be detached quickly upon high enough shear drag forces F_γ, the shear rate maxima are relevant for cross flow microfiltration. Therefore, the average of the periodic, shear rate maxima $\overline{\gamma}_{m,max}$ over the axial membrane length is extracted as the investigated membrane shear rate γ_m.

The simulation results at constant gap widths g over the full range of the rotational speed ω show that the shear rate maxima $\overline{\gamma}_{m,max}$ for each annular gap width scales linearly according to

$$\gamma_m(\omega) = a \cdot \omega + b \tag{9}$$

with fitting parameter arrays a and b dependent on the gap width g. It should be noted that this behavior is only valid for flow conditions above the critical Taylor number when flow instabilities are observed in the annular gap. Thus, $b \neq 0$ is valid for supercritical Taylor Numbers $Ta > 42$ [29].

Meanwhile, the average membrane shear rate $\gamma_{m,avg}$ scales with

$$\gamma_{m,avg}(\omega) = \alpha \cdot \omega^{\beta}, \tag{10}$$

where α and β are again fitting parameter arrays. An example of the simulation points and the corresponding function fits is given in Fig. 3**(b)**. While the membrane shear rate maxima $\overline{\gamma}_{m,max}$ are accurately approximated with a linear function, the average shear rate $\gamma_{m,avg}$ scales as a power function of the rotational speed ω, similar to the semi-analytical solution in [29]. The different shapes of the curves, and the inevitable convergence of both shear rates at a slightly higher than simulated rotational speed can be explained with the flow regimes in the Taylor–Couette cell. There is a clear difference between the shear rate maximum $\gamma_{m,max}$ and the average shear value $\gamma_{m,avg}$ in the presence of Taylor vortices. However, the regularly spaced Taylor vortices disappear at even higher Taylor numbers and the flow becomes fully turbulent, where shear rate peaks due to Kolmogorov microscale eddies can no longer be individually resolved by CFD on a reasonable mesh size. Since eddies smaller than cells are assumed to be very damaging to cells [31], this resolution limitation is not a concern.

A change of the annular gap width g influences the coefficient of the power function in Eq. (10), resulting in a variation of β between 1.5 and slightly below 2, as shown in Fig. 3**(c)**. The coefficient of the polynomial function is in good agreement with the analytical solution of the simplified Navier–Stokes equations in Eq. (8) for small gaps. However at larger numerical values of gaps g, there is a significant discrepancy of β, which gives rise to considerable differences in the expected average shear rate $\gamma_{m,avg}$, particularly at high speeds.

The results of the CFD simulations allow for a more precise calculation of the shear rate γ_m for the spinfilter, which is the most important parameter for the reduction of fouling and cake formation in cross-flow microfiltration [32].

In this parameter study, the rotating inner radius is maintained at a constant value. It is evident that a variation of r_m has a linear effect on the circumferential speed and, consequently, on the shear rate. However, other effects, such as on the coefficient β, are negligible as long as the size ratio of the Taylor–Couette cell remains approximately constant.

With two-dimensional, linear interpolation, a shear rate map, as illustrated in Fig. 4**(a)**, can be generated. A second round of simulations with operation points on the shear rate isolines allows for a direct comparison of the energy dissipation rate (EDR) distribution in the annular gap for equal flow behavior directly at the membrane. EDR serves as an indicator for the degree of cell damage by hydrodynamic stress and is further discussed in Section 2.4.

Experimental validation of the simulation results is conducted using a prototype (see Fig. 4**(b)**), wherein a cylinder is magnetically levitated and rotated in the fluid at a set rotational speed ω with two bearingless motors at its ends. The motors record the necessary drive current to

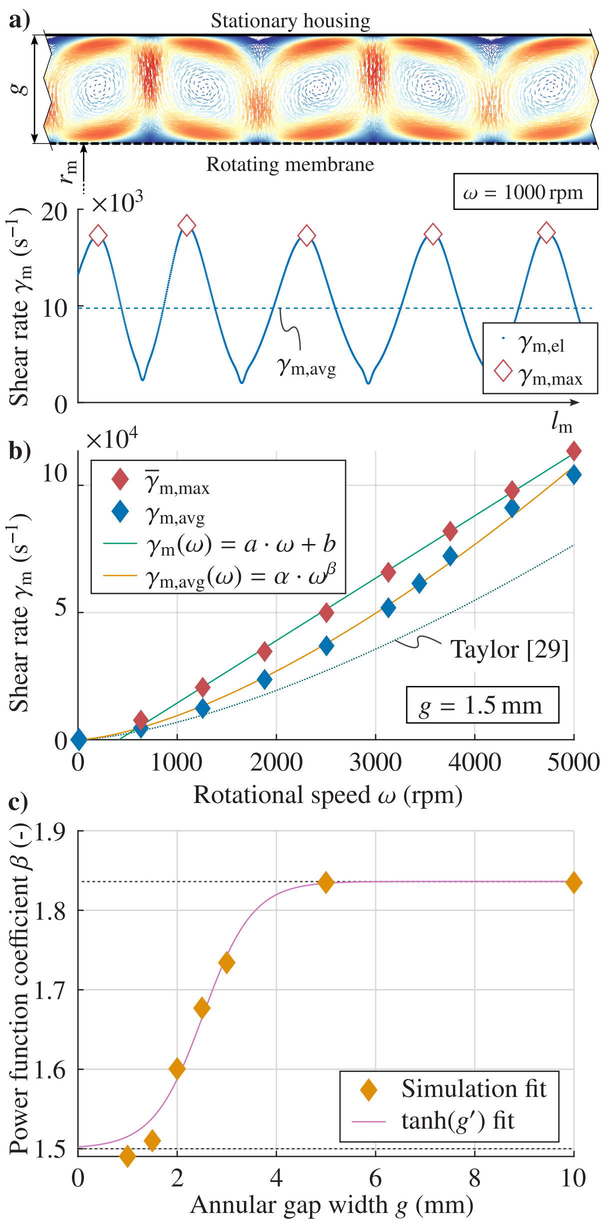

Fig. 3. Computational fluid dynamics (CFD) simulations allow to exactly determine the membrane shear rate γ_m. **(a)** The 2D-axisymmetric simulation domain is confined by the stationary housing wall on the outer cylinder and the membrane on the rotating inner cylinder. A simulation example of the center section with $g = 1.5\,\text{mm}$ and rotational speed $\omega = 1000\,\text{rpm}$ captures the Taylor vortices in the annular gap. The average of the periodic, local shear maxima $\bar{\gamma}_{m,max}$ at the membrane wall is the relevant shear rate for cross-flow microfiltration. **(b)** While the overall average shear rate $\gamma_{m,avg}$ of the simulated operation points show a similar behavior predicted in [29], the periodic maximum shear rate $\bar{\gamma}_{m,max}$ is more relevant for CFF and scales linearly with the rotational speed ω in the given range. **(c)** The power function coefficient β of Eq. (10) is fitted for each gap size g. For small annular gaps, the simulation results confirm Eq. (8), but deviate for larger values. A scaled tanh(g') fit varies with g between the analytical, lower bound to the empirically derived, upper bound.

maintain the set rotational speed ω. Consequently, the drive torque and shear rate can be calculated directly with the known dynamic viscosity of the fluid in the test cell. Two rotors of different lengths ($l_{r,1} = 50\,\text{mm}$ and $l_{r,2} = 100\,\text{mm}$) are subjected to testing, and the difference from one another is taken in order to compensate for the effects of the axial end faces and the cogging torque of the permanent magnet synchronous motors. The simulation is validated for water and a water-glycerine mixture at an elevated viscosity, thereby increasing

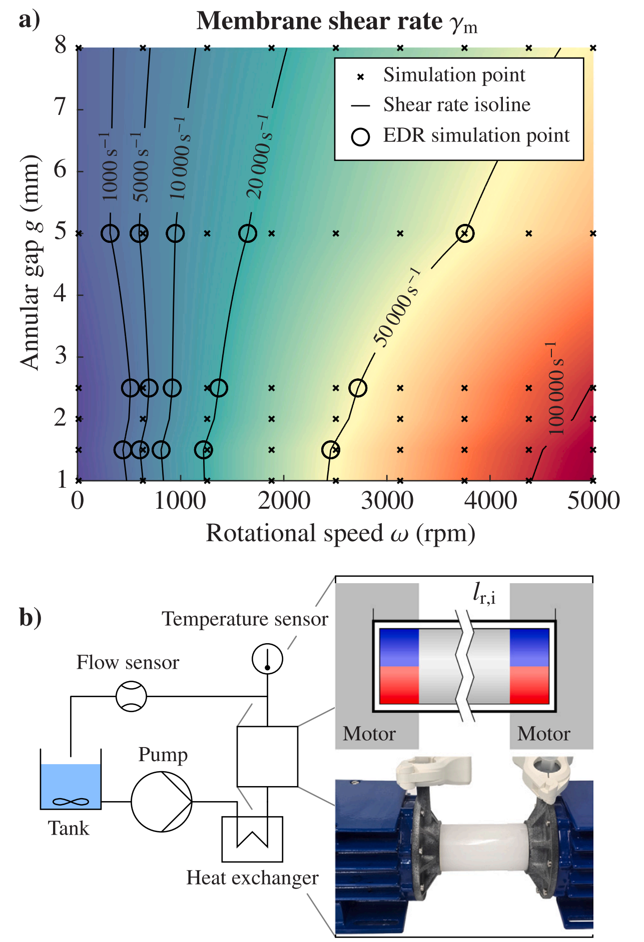

Fig. 4. **(a)** The dependence of the shear rate γ_m at the membrane surface is extracted from a simulation sweep of the variable parameters g and ω. A larger annular gap g generally requires a higher rotational speed to reach the same shear rate γ_m on the membrane to remove retained particles. A second set of simulations on the shear rate isolines, and therefore identical flow conditions in the vicinity of the membrane, reveals the distribution of the shear rate in the annular gap, from which the EDR of the filter module can be calculated. **(b)** The CFD simulations are validated on a test bench. A temperate-controlled water-glycerin mixture of adjustable viscosity is pumped in the annular gap of a levitating and rotating cylinder. The required drive current of the motors for constant speed control is measured directly from the bearingless motors, which allows to calculate the drive torque, and therefore the tangential shear rate on the cylinder surface.

the drive current signal. A small axial flow is superimposed by an external pump to prevent heating of the fluid which would reduce the viscosity of the fluid. The validation measurements corroborate the swirl shear rate component simulation results, exhibiting deviations within the expected range for CFD simulations.

In the passive flat plate filter module and the hollow fibers, the shear rate γ_m at the membrane is calculated with the spatial derivative of the pressure-driven Poiseuille flow profile in a rectangular channel or a round tube, respectively.

2.4. Energy dissipation rate

The damage to cells by hydrodynamic effects is frequently represented by the energy dissipation rate (EDR). The objective is to express the EDR of bioprocessing equipment as a scalar, thereby enabling a comparison of cell damage across a range of geometries and even processes. Often, it is of interest to determine the EDR limit at which cell cultures lyse [33]. However, sub-lethal responses, such as reduced protein production or glycosylation, are also important benchmarks for bioprocessing equipment [34]. The EDR response trigger limits allow to optimize the design of stirred bioreactors [35], centrifuges [36], microfluidic devices [37], and membrane filters [38].

The $\mathrm{EDR_{el}}$ can easily be extracted from CFD simulations according to

$$\mathrm{EDR_{el}} = \mu \nabla U_{\mathrm{el}} : \nabla U_{\mathrm{el}} \tag{11}$$

with the fluid viscosity μ and the fluid shear rate (strain) tensor ∇U_{el}.

However, the weighted reduction of the highly heterogeneous distribution of $\mathrm{EDR_{el}}$ in most investigated fluid domains is a great challenge and different methods have been applied in the past. In [39], the total EDR is determined by the median of the maximum $\mathrm{EDR_{tr}}$ along simulated particle trajectories. For the spinfilter in this work, particle tracking is not possible due to the reduction of the simulation space to a 2D-axisymmetric domain. Another approach, that has shown to agree well with the particle trajectory method, is the flow-weighted EDR through an artificial cross section [40]. Since the module-wide through-flow of the spinfilter is the superimposed, axial annular flow, the EDR of the spinfilter could be weighted in a similar manner with the flow profile

$$v_{\mathrm{ax}}(r) = \frac{G}{4\mu}(r_m^2 - r^2) + \frac{G}{4\mu}(r_{\mathrm{o}}^2 - r_{\mathrm{m}}^2)\frac{\ln(r/r_{\mathrm{m}})}{\ln(r_{\mathrm{o}}/r_{\mathrm{m}})} \tag{12}$$

with the axial pressure drop $G = -\frac{dp}{dx}$, which is based on the retentate flow Q_{ret}, and the fluid viscosity μ [41]. However, the axial flow with $Q_{\mathrm{ret}} = 150\,\mathrm{mL\,min^{-1}}$ is so low compared to the heavy, internal mixing due to the Taylor vortices. Thus, the idea of weighting the EDR on the through-flow makes less sense if the mixing along the fluid trajectory is strong and all cells are expected to be exposed to all flow conditions within the fluid volume. Consequentially, the flow-based weighting matrix coefficients for the spinfilter approaches unity gains. Numerically speaking, the flow-weighting method yields a lower, overall EDR since the through-flow is lower near walls, where the shear rate is typically higher. Meanwhile, the method used here with unity weights most likely overestimates the impact of high shear rate regions near walls with little through-flow contribution. Conservatively, the unity weights set a stricter limit for the maximum permissible rotational speed of the spinfilter. Finally, the EDR for the spinfilter is given as

$$\mathrm{EDR} = \mu \sum_{\mathrm{el}} W_{\mathrm{el}} V_{\mathrm{el}} (\nabla U_{\mathrm{el}} : \nabla U_{\mathrm{el}}) \tag{13}$$

with the weights $W_{\mathrm{el}} = I$ (or $W_{\mathrm{el}} \propto v_{\mathrm{ax}}(r)$ according to Eq. (12) as a comparison), the element volumes V_{el}, and again the fluid viscosity μ and the strain tensor ∇U_{el}.

The EDR of the spinfilter at varying operational points can be evaluated in conjunction with existing research to anticipate the response of different cell cultures. In particular, the comparison is employed to identify the maximum permissible rotational speed for the spinfilter for specific cell lines.

3. Experimental

The particle force model presented in Section 2 is subjected to experimental validation. A spinfilter prototype serves to determine the optimum operating point with regard to the maximum filter flux in a series of tests utilizing different membrane nominal pore sizes and media, and is compared to a flat plate passive TFF reference system. Furthermore, hemolysis tests are conducted to compare the degree of cell damage caused by the spinfilter and a commercial hollow fiber filter.

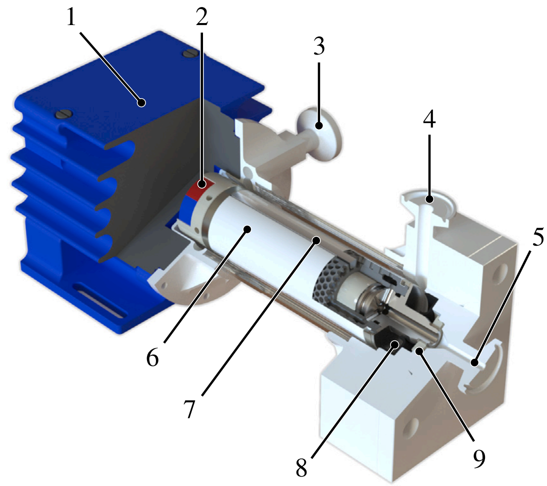

Fig. 5. The spinfilter prototype with an integrated lip seal between the feed and the filtrate decouples the shear rate γ_{m} on the membrane from the TMP, which allows to set both parameters independently of each other. A partial cross section shows the internal components of the spinfilter. (1) Bearingless motor (2) Permanent magnet (3) Feed inlet (4) Retentate outlet (5) Filtrate outlet (6) Rotor with the filter membrane (7) Adhesive-free membrane attachment system with a titanium wedge (8) PTFE lip seal (9) Hydrodynamic bearing on the filtrate side.

3.1. Spinfilter prototype

To test and identify the optimal ratio between the orthogonal and parallel forces according to the particle force model, the TMP must be adjustable independently of the shear rate γ_{m} at the membrane. Earlier prototypes of bearingless spinfilters [22] inevitably feature an open gap between the feed and the filtrate. Different topologies, including labyrinth seals and integrated impellers, generate a pressure differential within the module and prevent internal leakage through dynamic pressure compensation. However, for any spinfilter prototype with a co-rotating impeller, the TMP-γ_{m} ratio is limited to the one-dimensional input of the rotational speed ω. A prototype incorporating an FDA-certified PTFE lip seal (Dichta AG, Balerna, Switzerland) between the feed and the filtrate is capable of sealing the open gap, even in the event of an uncompensated pressure differential. To satisfy the stringent concentricity requirements of the lip seal, a hydrodynamic bearing machined from iglidur H (igus GmbH, Cologne, Germany) is designed according to [42] and installed on the cell-free filtrate side instead of a secondary magnetic bearing. Although the spinfilter operation is no longer completely contactless, the primary advantages of the bearingless spinfilter concept remain, with a hermetically sealed housing and the absence of a rotational seal to the environment. Fig. 5 visualizes a partial section cut of the prototype, in which the primary components are indicated. The housing of the filter module is milled from POM-C, and all wetted surfaces are polished, as cell lysis is strongly linked to surface quality [43]. The rotor shaft in contact with the lip seal is manufactured from plasma-nitrided, medical-grade stainless steel (1.4401). The membrane support structure is 3D printed due to its geometrical complexity. However, the entire surface is completely covered by the membrane, thereby ensuring that no rough surface comes into contact with the cell culture. A commercial polyethersulfone (PES) filter membrane (Sterlitech, Auburn, WA, USA) in three different nominal pore sizes (0.2 μm, 0.8 μm and 8 μm) is used and clamped onto the outer surface of the rotor with a titanium wedge in an adhesive-free clamping mechanism. The active membrane area in the spinfilter is $44\,\mathrm{cm^2}$. The rotor is driven by a bearingless motor (Levitronix, Zurich, Switzerland) with a customized firmware, which accounts for the rotor dynamics of the filter, including the hydrodynamic bearing.

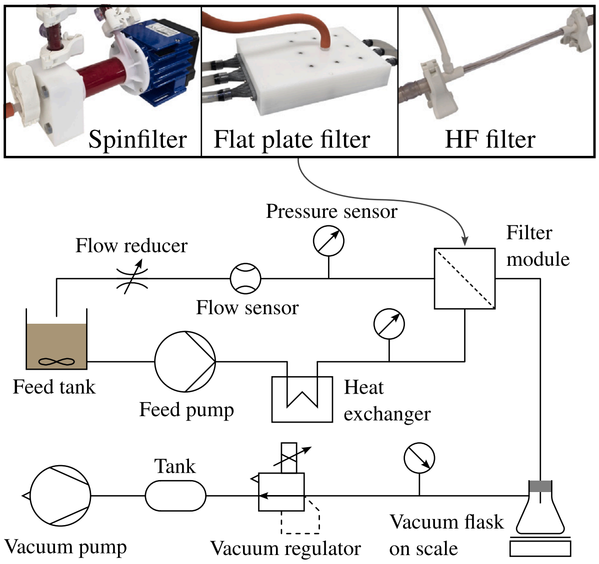

Fig. 6. The spinfilter and reference filter modules are tested within the same fluid circuit to ensure comparable measurement results. However, depending on the filter type, some components must be exchanged to accommodate the specific requirements of a certain filter module. The stirred feed tank ensures that the suspension stays homogeneous. The feed fluid is pumped through the filtration modules, where Q_{ret} is adjusted depending on the tested filter type. The fluid is temperature-controlled in a heat exchanger. Both the pressure and the fluid flow are measured and digitally recorded. An external pressure p_{ext} is applied by a closed-loop electronic vacuum regulator on the filtrate side. The filtrate flow is then measured on a precision scale.

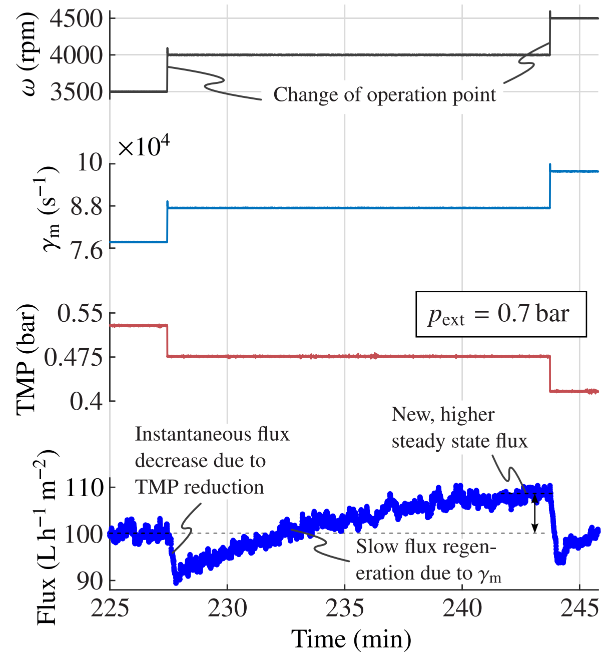

Fig. 7. An excerpt of the measurement procedure demonstrates the temporal dependence of the filter flux with respect to the ratio of the TMP and the membrane shear rate γ_m. Starting from a constant filtrate flux at the operation point at 225 min of the measurement series, the rotational speed ω is increased to 4000 rpm, which consequently increases γ_m and decreases the TMP due to the centrifugal pressure of the filtrate. An instantaneous decrease of the filter flux is observed, as the TMP is reduced. Over the time span of approximately 15 min, the filtrate flux is regenerated, since the higher shear rate γ_m removes more of the retained particles from the membrane surface. Once the new steady state operation is reached, the new filter flux is recorded and the rotational speed is increased again.

3.2. Reference systems

A passive TFF module with the same filter membranes as the spinfilter is designed in parallel. The flat plate module features a rectangular channel of height $h_{ch} = 0.85$ mm, membrane width $w_{ch} = 100$ mm and membrane length $l_{ch} = 100$ mm with the membrane attached to one wall surface. The module is manufactured from POM-C and the wetted surfaces are polished. The feed and retentate flows are introduced to the module in parallel via tubing splitters, which ensure uniform flow distribution for the high aspect ratio channel. Furthermore, the design accounts for the laminar formation length of the Poiseuille flow prior to the feed flowing over the membrane surface.

For the hemolysis tests, the spinfilter is compared to a hollow fiber module with a 0.2 μm PES membrane (Repligen, Waltham, MA, USA) with a filter area of 88 cm^2 and inner fiber diameter of 1 mm.

3.3. Fluid circuit

The spinfilter prototype and reference systems are operated within the fluid circuit depicted in Fig. 6, in which the TMP can be adjusted with a feedback-controlled vacuum pressure valve (SMC Co., Chiyoda, Japan). A peristaltic pump (Cole-Parmer, Vernon Hills, IL, USA) continuously exchanges the feed within the filter module. The pump is calibrated with an inline flow sensor (Levitronix GmbH, Zurich, Switzerland). In the experiments with the spinfilter, where the shear rate is decoupled from the retentate flow, the feed pump is operated at a low speed with retentate flow $Q_{ret} = 150\,\mathrm{mL\,min^{-1}}$. A water-immersed heat exchanger regulates the temperature of the feed fluid to 25 °C. The filtrate flow is measured in real time via a suction bottle on a precision balance (Kern & Sohn GmbH, Balingen, Germany). To prevent a significant change in the feed particle concentration, the suction bottle is emptied at regular intervals.

The fluid circuit for the reference modules is conceptually identical to that of the test setup of the spinfilter. However, due to the higher retentate flow required for passive TFF, a more powerful pump (Levitronix GmbH, Zurich, Switzerland) is employed, and tubing and in-line sensors with a larger cross-section are utilized. A flow sensor (Levitronix GmbH, Zurich, Switzerland) measures the retentate flow, from which the shear rate is calculated. A pressure sensor (Pendotech, Plainsboro, NJ, USA) positioned in the feed at the midpoint of the membrane overflow length provides an average measurement of the TMP, which serves as the feedback control quantity for the centrifugal pump. The shear rate can be decoupled from the TMP by partially clamping the retentate tubing. The filtrate flow is once again measured with the same balance as previously described.

3.4. Operating point measurements

Baker's yeast, *Saccharomyces cerevisiae*, (Merck, Darmstadt, Germany) at a concentration of $5\,\mathrm{g\,L^{-1}}$ in DI water serves as a cost-effective substitute for a biotech cell culture. Prior to testing, all newly installed membranes are subjected to a preliminary loading phase at the maximum permissible operating pressure $p_{lim} = 0.7$ bar and a low shear rate, until no measurable change in the filtrate flow rate is observed. The typical duration of this process is approximately 3 h.

An exemplary illustration of the measurement sequence is provided in Fig. 7. Once a steady state has been reached with regard to the filtrate flux for a set TMP and shear rate γ_m, the rotational speed ω is increased. Consequently, the TMP declines, resulting in an immediate reduction of filtrate flow. However, due to the higher shear rate, the filtrate flow regenerates over a period of typically 15 min. Once the new steady state is reached, the operating point is averaged and recorded for one minute. Subsequently, a new operating point is set.

The operating points are controlled with a sequential decrease in external pressure difference and an increase in rotational speed (or an increase in retentate flow for the passive tangential flow module) such that the effect of internal pore blocking, which increases over time, is minimized.

3.5. Hemolysis tests

Freshly drained bovine blood from a local slaughterhouse is used for the hemolysis tests. 25 mL L^{-1} of Oaxlate anticoagulant is added directly at the slaughterhouse. Experiments are performed with the original blood and a 1:4 dilution in phosphate-buffered saline (PBS), which reflects the typical cell concentration in perfusion. To prevent osmotic shock, the fluid circuit is pre-flushed with isotonic PBS. Prior to filtration measurements, static control samples are collected and stored at a temperature of 30 °C. The hemolysis tests are carried out at a constant TMP = 0.7 bar and a fluid temperature of 30 °C. The rotational speed ω of the spinfilter, or the retentate flow Q_{ret} of the HF filter is increased in 30 min intervals. Given that the TMP of the spinfilter is dependent on the rotation speed, the vacuum pressure p_{ext} is adjusted accordingly. A blood sample is collected every 15 min and centrifuged in two stages for 10 min at 3070 g each. The resulting supernatant is analyzed using Drabkin's method in a photo spectrometer (Thermo Fischer Scientific, Waltham, MA, USA) at 540 nm. The quantity of plasma-free hemoglobin (PFH) released due to cell wall ruptures of red blood cells induced by hydrodynamic stress is quantified for each operating point.

4. Results

This section presents the results of the operating point determination and the hemolysis tests of the spinfilter, which are compared with the model and the reference system.

4.1. Particle force model

A comparison between the particle force model and the measurement data is presented in Fig. 8 after fitting the open scalar parameters to the measurement data. Given that the TMP is dependent on the rotational speed ω, a region of negative TMP exists at high speeds and low pressures. Conversely, operation at high vacuum pressures and low rotational speeds is constrained by the membrane's burst pressure p_{lim}. The model demonstrates the greatest degree of alignment with the measurement data when a very wide normal distribution of the particle size is assumed. The size distribution of the yeast cells is corroborated by a cell counter (Logos Biosystems, Dongan-gu, South Korea), as seen in Fig. 9. In addition to the modeled Gaussian distribution of yeast cells, there is a significant presence of smaller particles, which may include cell fragments of broken cells. Consequently, for efficient cross-flow filtration, the shear rate must be not only sufficient to remove the intended cells from the membrane, but also significantly higher to detach the smaller particles from the membrane. This is due to the fact that the shear-induced drag force, as described in Eq. (3), scales with the particle size.

The impact of the membrane pore size is compared in Fig. 10**(a)** to **(c)**, where the filter flux is plotted against the TMP at discrete rotational speeds.

As the model predicts, the filtrate flux in Fig. 10**(a)** and **(b)** scales linearly with the TMP as long as the shear rate is sufficiently high to remove the retained particles. Otherwise, the filtrate flux stagnates when the membrane is covered in a cake layer that increases the flow resistance. An increase in the spinfilter's rotational speed enables a broader operational range of approximately linear filter flux behavior. As can be observed in Fig. 10**(c)**, the membrane with a nominal pore size of d_{pore} = 8 μm exhibits no significant influence of the rotation speed ω on its filtration performance. Given that the nominal pore size d_{pore} = 8 μm for this membrane is larger than the average particle size d_p = 6.1 μm, this result is to be expected. The particles can readily enter the pores and block the membrane pore structure

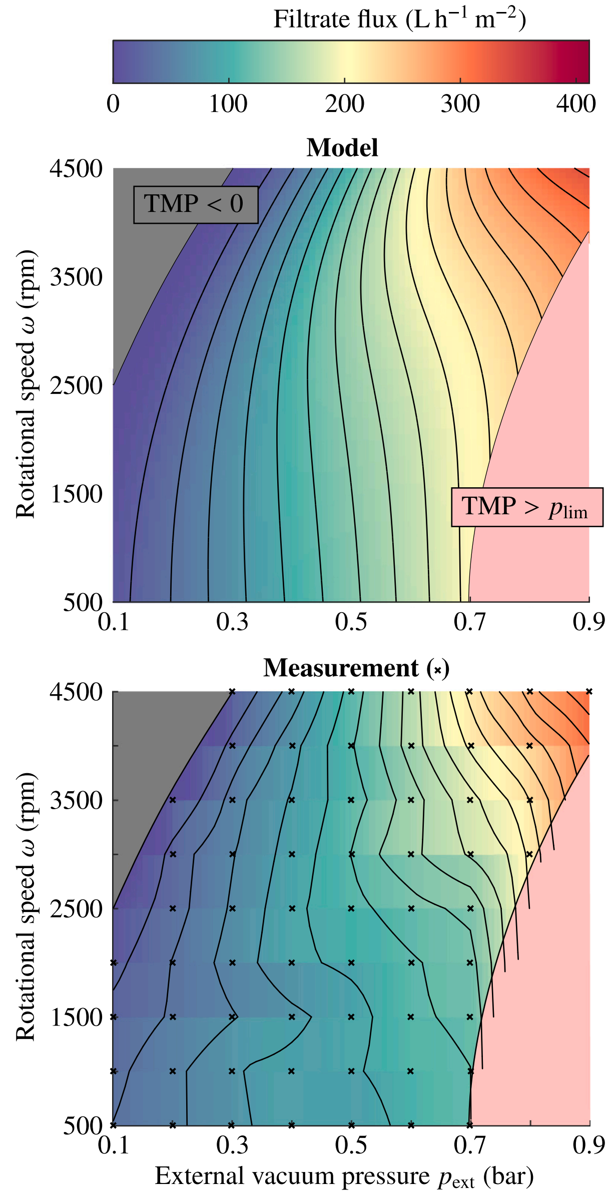

Fig. 8. The open model parameters are adjusted according to the measurements and compared to each other for the membrane with d_{pore} = 0.8 μm. Due to the centrifugal pressure depending on the rotational speed ω, the TMP for high values of ω and low external pressures p_{ext} is negative. On the other hand, the measurement region is limited by the burst pressure p_{lim} = 0.7 bar of the membrane. The best fit is found for λ_{fr} = 2 and a wide particle detachment region, indicating that the tested cell suspension contains not only the target cells, but additional components.

internally, where they are unaffected by superficial shear drag forces. This behavior is corroborated with SEM images of the membrane cross section, which reveal the deposition of yeast cells within the membrane structure shown in Fig. 11. Despite the fact that cells can enter the large pores, after some initial impurity in the permeate, no particles have been detected after a while of operation. This effect may originate from particles that block pores internally and thus reducing the effective pore size d_{pore} that prevents more particles from traversing the membrane. Note that all measurements in Fig. 10**(a)** to **(c)** points are measured with a pre-loaded membrane, where the membrane has been exposed

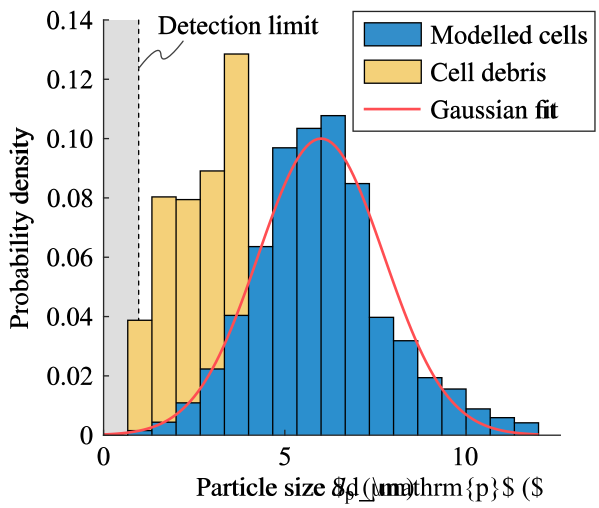

Fig. 9. The yeast suspension particle size distribution is analyzed and split into the modeled cell size distribution according to a Gaussian distribution and additional particles such as cell debris detected by the cell counter. Since the cell counter cannot reliably resolve particles below 2 μm, the deviation of the real distribution compared to the model might be even larger. The removal of smaller particles than the expected cells necessitates the application of a higher shear rate γ_m.

to the feed at the maximum TMP for multiple hours, and especially the 8 μm membrane is already heavily blocked internally. In contrast, the base permittivity of a fresh 8 μm membrane is significantly higher than the membranes with smaller pores for the flux of pure water.

Fig. 10**(d)** illustrates the relationship between the filtrate flux with respect to the ratio of the shear drag force to the filtration force. A clear trend is evident that the filter flux is greater for higher force ratios. However, no distinct inflection point can be identified that would suggest the existence of a specific force ratio, or static friction coefficient, at which particles clearly detach from the membrane. This is likely due to the broad size distribution of the cells and pores in reality. Moreover, the rotational speeds are separated horizontally, indicating that the shear drag force F_γ is underweight in the model or the filtration force F_TMP is overweight.

4.2. Reference system comparison

To facilitate a comparative analysis of the spinfilter and the passive TFF flat plate filter, it is necessary to present the measurement data in a different format. Instead of the TMP on the horizontal axis, the rotational speed ω or the shear rate γ_m, respectively, is plotted on the x-axis in Fig. 12**(a)**, while the TMP is binned into discrete levels. The filter flux is normalized for each discrete TMP step, which permits a direct comparison between the operational points. This representation again corroborates the model's flux prediction: at low TMPs, such as 0.1 bar, the shear rate exerts a negligible influence on filter performance, as few particles are deposited on the membrane at this filtration force. At higher TMP however, a greater shear rate is required to remove the retained particles from the membrane, resulting in an increase in filter flux at higher shear rates.

The inset shown in Fig. 12**(b)** presents a direct comparison between the spinfilter and the flat plate filter module. First, it is evident that the passive TFF module is unable to reach the high shear rates achieved by the spinfilter, as the maximum retentate flow rate $Q_\mathrm{ret,lim} = 15\,\mathrm{L\,min^{-1}}$ is constrained by the feed pump power limitation. Therefore, the region where the shear rate begins to affect the filtration performance cannot be accessed.

The clear, quantitative difference, despite the same average TMP and shear rate on the membrane of both filter modules, is explained by the fact that a large pressure difference of over 0.5 bar occurs in the passive TFF module over the rectangular channel length at high retentate flows. As a consequence, the filter membrane is subjected to highly unequal loading. Close to the feed inlet of the filter, the TMP is excessively high, resulting in the majority of particles adhering to the membrane and severely restricting the filter flux locally. Conversely, on the retentate side of the membrane, there is virtually no TMP remaining, leading to a similarly low filter flux on this region of the membrane. Only a narrow zone of the flat plate filter membrane in the center with respect to the feed flow direction is subject to the set conditions, whereas in the spinfilter, the whole membrane surface is loaded equally. The quantitative advantage of the dynamic membrane over the static membrane can therefore be expressed as the ratio between the filtrate fluxes, which is greater than threefold.

4.3. Hemolysis

A potential application of the spinfilter is the continuous separation of proteins from cell cultures during perfusion. The cells are to be retained by the filter and returned to the bioreactor, while the produced proteins and antibodies shall be separated and forwarded to the downstream process. It is essential that the live cells survive the separation process and are able to continue production. In this study, hemolysis tests of the spinfilter and a reference hollow fiber filter quantify the degree of cell damage caused by hydrodynamic stress during cross-flow filtration.

The results for the separation of red blood cells from the undiluted bovine blood are presented in Fig. 13**(a)**. Curiously, the filtrate flow in the hollow fiber filter demonstrates a decline with an increasing shear rate. This phenomenon likely originates from the high viscosity associated with the particle concentration at a hematocrit $Ht = 41\%$, which results in a considerable pressure drop along the length of the hollow fibers. In addition to the static viscosity of the blood, shear thickening effects of the non-Newtonian fluid amplify this effect.

The degree of cell damage is quantified by plasma-free hemoglobin (PFH) per volume filtrate in Fig. 13**(b)**, where the spinfilter demonstrates a notable reduction in cell damage compared to the hollow fiber filter. At lower shear rates, where the majority of retained particles remain attached to the membrane, the degree of cell damage exhibits a linear behavior. However, once the shear drag force is sufficiently high to detach the red blood cells from the membrane, the efficiency is enhanced significantly. Consequently, the same volume of filtrate can be filtered in a shorter time, thereby reducing the exposure time of the cells to the filtration process. Operating the spinfilter at high speed ω not only reduces the overall separation process time but also improves the cell viability per volume of filtrate at the optimal operating point.

For diluted blood, where the cell concentration assumes a realistic value also encountered in perfusion [14], the shear rate, as illustrated in Fig. 14**(a)**, no longer exerts a filtrate flow reducing effect for the hollow fiber filter. However, the filter performance does not exhibit a notable increase either.

With regard to cell damage in Fig. 14**(b)**, the photo-spectrometric signal in diluted blood is considerably weaker, and measurement errors contribute to substantial relative inaccuracies. Particularly at low shear rates, no definitive conclusion can be drawn for the degree of cell damage in both filter modules.

At higher shear rates, however, a trend similar to that observed for undiluted blood emerges. The enhanced filter performance in the spinfilter effectively offsets the increased cell damage rate due to the higher shear stress. Therefore, the relative cell damage per volume filtrate is significantly lower compared to the hollow fiber filter with a shorter process time.

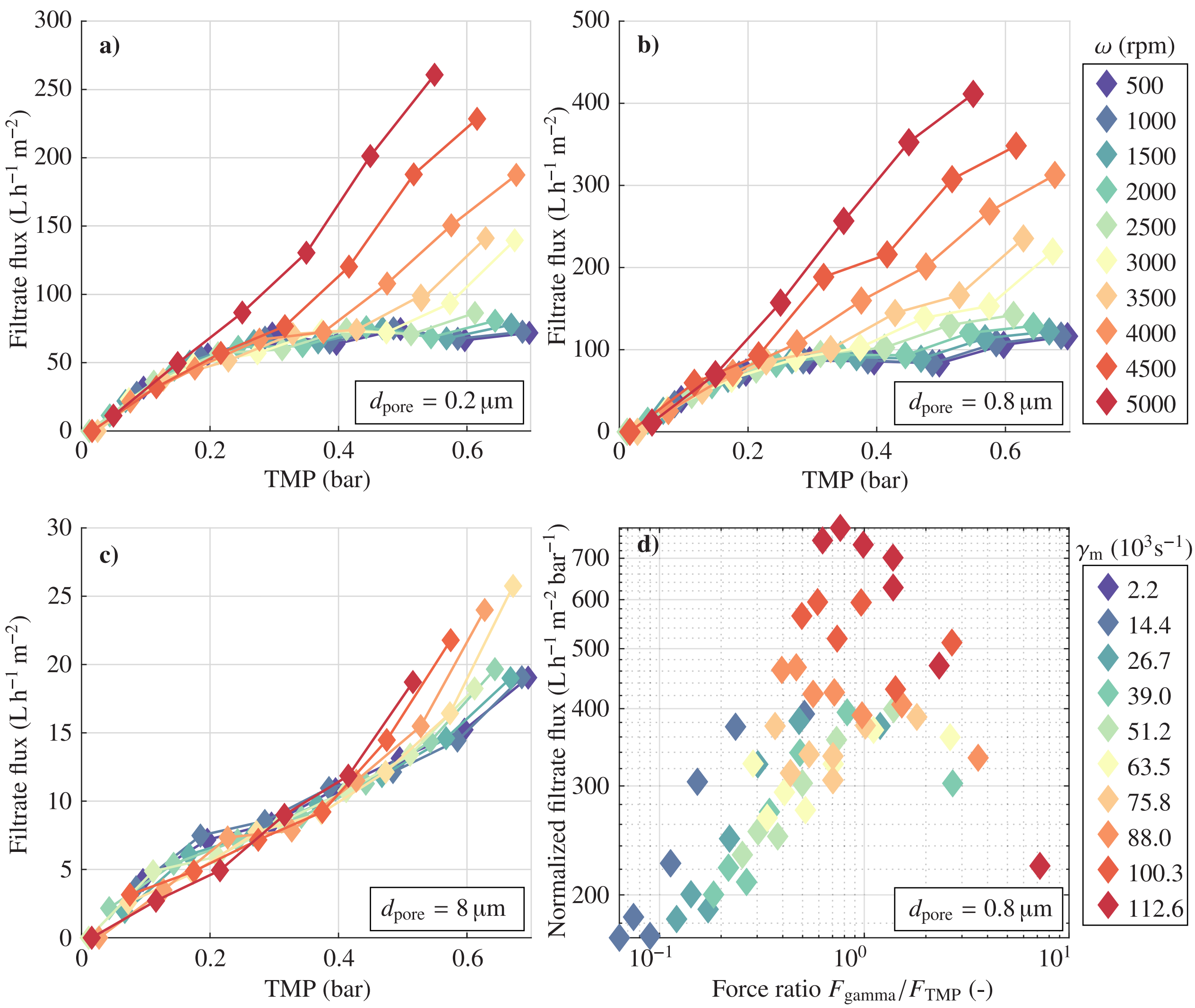

Fig. 10. Measurement results for all membranes with different pore sizes are plotted against the TMP for discrete levels of the rotational speed ω, and thus shear rate γ_m. **(a)–(b)** For the membranes with $d_{pore} = 0.2\,\mu m$ and $d_{pore} = 0.8\,\mu m$, the filter flux increases with TMP until the particles cannot be removed by the specific shear rate γ_m anymore. For higher γ_m, the approximately linear dependency of the filter flux on the TMP continues for a wider range. The membrane with the larger pores allows for a generally higher flux. **(c)** The rotational speed and shear rate has no meaningful influence on the filter flux of the membrane with $d_{pore} = 8\,\mu m$. Since $d_{pore} > d_p$, the particles can easily enter and internally block the membrane, where they are no longer affected by the superficial shear rate. Despite the large pore openings compared to the other membranes, the filter flux is an order of magnitude smaller. Curiously, the filtrate has still shown a purity that is indistinguishable from the other experiments. **(d)** The filter flux for the membrane with $d_{pore} = 0.8\,\mu m$ is shown on a logarithmic scale in dependence of the force ratio between F_{TMP} and F_γ. It is evident that a higher force ratio leads to a higher filter flux, but the horizontal separation of the operation points with respect to the membrane shear rate γ_m indicates some deficiencies in the model. Without any pore and particle size distributions, a sharp bend is expected, where the bending point would indicate the friction coefficient λ_{fr}. However, due to the wide particle size distribution, any potential particle detachment condition is heavily attenuated.

4.3.1. EDR simulations

A comparison of the simulation results on the membrane shear rate isolines for different gap widths shows that a wider gap g leads to a lower total EDR in the spinfilter at higher shear rate levels, as illustrated in Fig. 15.

Given that an elevated shear rate on the membrane has been demonstrated to result in enhanced filter fluxes, the optimal operational point of the rotational filter is at the limit, where cell responses are triggered. Whether this limit is the lethal or sub-lethal response is contingent on the production process. Close to the permissible EDR limit, higher membrane shear rates γ_m are possible for larger gaps g. Nevertheless, a greater gap results in a larger fluid hold-up volume outside the bioreactor, which is typically undesirable in bioprocessing equipment. Especially for low-volume applications such as patient-customized therapeutics, the volume in any filter must be kept small.

It should be noted that for lower membrane shear rates γ_m, the increased fluid volume at wider gap widths leads to higher EDR results. This trend might indicate that the distribution of the shear rate is less

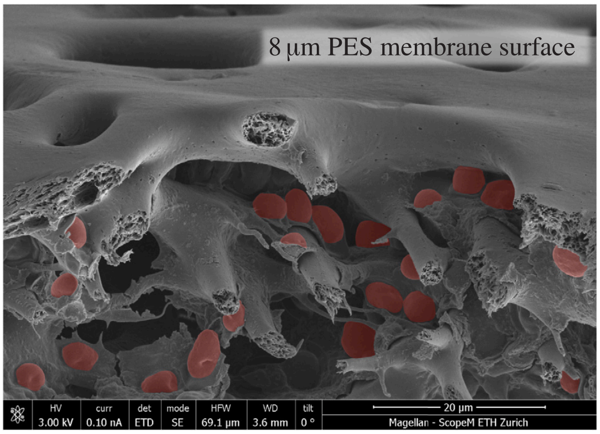

Fig. 11. A cross section of the membrane with pores $d_{pore} = 8\,\mu m$ is analyzed by a scattering electron microscope, where many retained particles within the pore structure of the membrane are found and indicated in red. Note that the membrane has been air dried after the filtration experiment with yeast. Therefore, the yeast particles have shrunk considerably and appear smaller than their size during the filtration tests.

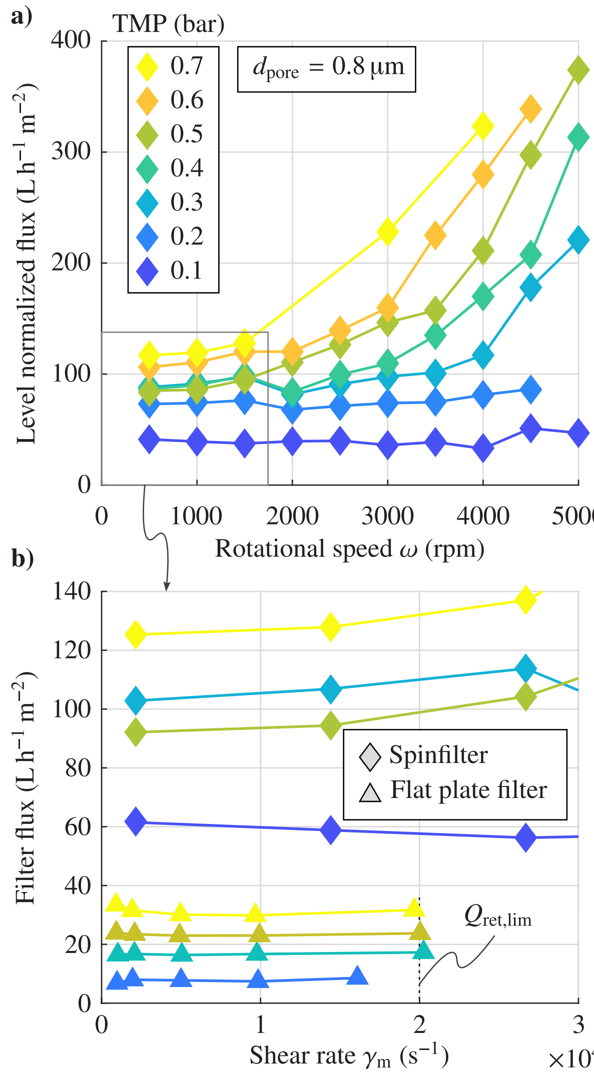

Fig. 12. **(a)** The spinfilter flux measurements for the membrane with $d_{pore} = 0.8\,\mu m$ are plotted against the rotational speed, or the shear rate γ_m, respectively, while the TMP at each measurement point is binned in discrete steps of 0.1 bar. An increase of the shear rate γ_m leads to an increase in filter flux for higher TMPs, where the higher shear rate allows to remove even the smaller, retained particles. On the other hand, for lower TMPs such as 0.1 bar, most of the particles are already removed at the lowest rotational speed with $\gamma_m = 3000\,s^{-1}$ of the experiment, thus the higher shear rates show no additional effect on the flux. **(b)** The spinfilter is compared to the flat plate reference filter module. First, the maximum shear rate in the flat plate filter is limited to approximately $20\,000\,s^{-1}$ due to power limitations of the feed pump at $Q_{ret,lim} = 15\,L\,min^{-1}$. Thus, the region where the membrane shear rate γ_m shows a significant effect on the filter flux in the spinfilter cannot be reached in the reference filter. Moreover, a huge pressure drop over the length of the module is observed, which leads to a highly uneven load distribution on the membrane. The result is a reduced filter flux of a factor of approximately threefold.

favorable for larger volumes. Alternatively, the EDR calculation method might need improvement with a weighting matrix $W_{el}(\nabla U el)$ dependent on the strain tensor itself.

5. Conclusion

A bearingless spinfilter shall be operated at the optimal operating point with respect to the TMP and the shear rate γ_m at the membrane surface. CFD simulations allow for the precise calculation of the shear rate γ_m and the EDR distribution within the rotating annular gap. The simulation results are validated with experiments and compared to literature. A particle force model adapted for the spinfilter is capable of predicting the detachment condition of retained particles. This can then be employed to predict the filter flux through the membrane. Three open scalar parameters are adapted to the measurements for this purpose: the static friction coefficient λ_{fr}, the constant surface energy force F_{charge}, which depends on the chemical nature of the membrane and the components of the suspension, and the slope of the cumulative particle detachment probability, which depends on the size distribution of the particles and membrane pores. Given the considerable range of particle sizes that are typical of biotechnology suspensions, the effects of the model are significantly attenuated. Nevertheless, the model demonstrates robust predictive capabilities with regard to the behavior of the filter, provided that the particles in question are of a size significantly larger than that of the membrane pores.

A spinfilter prototype, actuated by a bearingless motor and equipped with an integrated lip seal between the feed and filtrate, is employed to conduct experimental measurements with a yeast cell culture and bovine blood, with the objective of determining the optimal operating point. In general, an increase in the filter flux is observed with an increase in both the TMP and the shear rate γ_m on the membrane. Additionally, the ratio of these two values plays a significant role. Since mammalian cells ($d_p = 15\,\mu m$ to $20\,\mu m$) are significantly larger than yeast cells, the filter mechanics are also affected by other cells, the filter dynamics are also affected in two ways. First, it was shown that the pore sizes d_{pore} must be smaller than the particle diameter d_p to avoid internal pore blockage in the interior of the membrane. Larger suspended particles will allow for membranes with larger pores, which generally increases the base membrane flux, and thus the filtration performance. Moreover, larger particles are quadratically affected by the shear drag force f_γ, while the orthogonal forces scale with the pore size d_{pore} only. According to the particle force model, the expected permeate flow for mammalian cells is therefore higher than with the yeast cell culture.

Hemolysis tests demonstrate that the optimal operating point of the spinfilter must not be determined exclusively on the basis of the filter flux, but also on the distribution of the shear rate in the annular

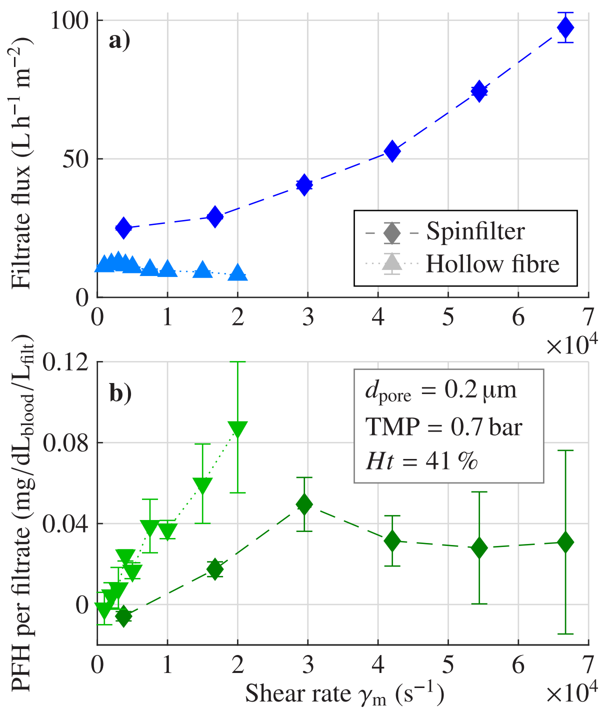

Fig. 13. Bovine blood is filtered with both the spinfilter and the hollow fiber filter of equal nominal pore size $d_{\mathrm{pore}} = 0.2\,\mu\mathrm{m}$ at a constant (average) TMP = 0.7 bar. **(a)** Similar to the yeast experiments, the spinfilter flux increases with increasing membrane shear rate γ_{m}. However, the contrary is observed for the hollow fiber module: Due to the high particle concentration of undiluted blood with a hematocrit $Ht = 41\%$, the fluid viscosity is high and non-Newtonian, which leads to a large pressure drop for higher retentate flows Q_{ret}, and thus uneven membrane loading, over the length of the fibers. Ultimately, this reduces the total filter flux for higher shear rates γ_{m}. **(b)** The plasma-free hemoglobin (PFH) per volume filtrate is compared for both filter types, which indicates the degree of hydrodynamic stress on cells. For the hollow fiber filter, a higher shear rate leads to higher levels of cell damage. For the spinfilter, the same effect is observed for an increase in rotational speed ω, however, once the particle detachment region is reached, the filter flux scales faster than the degree of cell damage, which leads to a reduction of cell damage per volume filtrate. Additionally, the process time at the operation points of higher shear rates lead to shorter process times.

gap. It is crucial to generate exactly the required shear rate on the membrane surface for a given TMP in order to separate cells from the produced proteins as gently as possible. Any deviation from the optimal operation point leads to unnecessary hydrodynamic stress on the cell culture. The spinfilter can separate red blood cells from blood plasma with less cell damage in a shorter process time when operated at the optimal rotational speed and TMP compared to a hollow-fiber filter based separation process.

Using the calculated EDR for the spinfilter in a comparison with measurements from the literature, it is possible to determine the maximum permissible rotational speed ω for biotech-relevant cell cultures such as CHO cells. For the spinfilter prototype with a gap width g = 1.5 mm, the spinfilter rotational speed ω is limited to 2000 rpm to avoid a change in glycosylation pattern for a commonly used CHO cell culture. Since this limit is specific to the cell culture, new measurements would have to be conducted for other applications of the bearingless spinfilter in biotechnology.

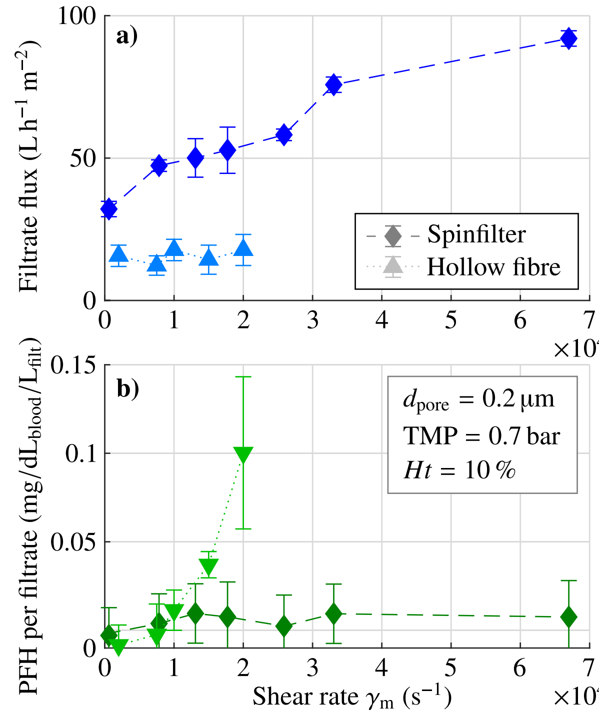

Fig. 14. The hemolysis test is repeated for diluted blood with a hematocrit $Ht = 10\%$, which reflects the typical particle concentration encountered in perfusion. **(a)** Again, the spinfilter flux increases with a higher shear rate on the membrane. For the hollow fiber filter, the flux is approximately constant, indicating still a highly uneven membrane loading, even though the pressure drop over the fiber length is reduced compared to the undiluted blood. **(b)** The degree of cell damage in the hollow fiber filter application behaves similarly to the experiment with undiluted blood, where higher membrane shear rates γ_{m} lead to more free hemoglobin in the blood plasma. For the spinfilter, an increased level of hydrodynamic stress in approximately compensated by the more efficient filtration process at higher rotational speeds ω. However, the relative error of the spectral absorbance measurement is larger for the diluted blood, leading to less robust results.

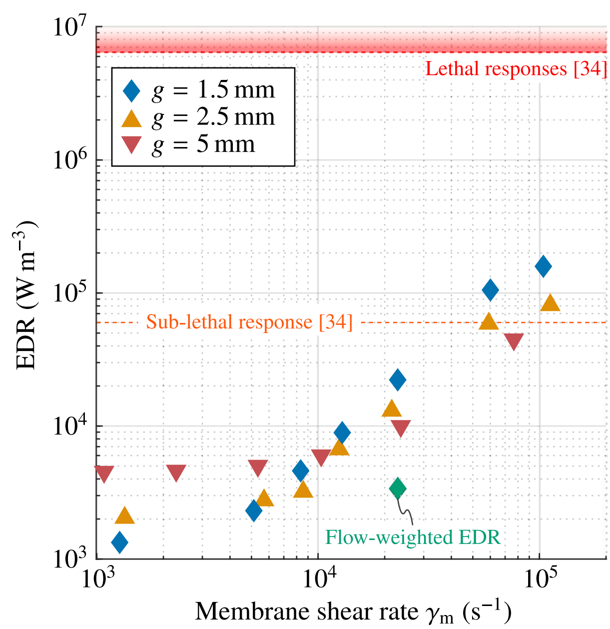

Fig. 15. The cumulative EDR for different gap widths g shows that a wider gap leads to less hydrodynamic damage on the cells for the same flow conditions directly at the membrane, given by the shear rate γ_{m}. While all simulation points are clearly below the lethal responses reported in [34], a stricter limit of a shifted glycosylation pattern of CHO cells at EDR = 6.4×10^4 W m^{-3}. Additionally, an example of the flow-weighted EDR is given for the gap width $g = 1.5$ mm, which is shown to be almost an order of magnitude lower than the unity-weighted calculation.

Declaration of competing interest

The authors declare the following financial interests/personal relationships which may be considered as potential competing interests: Lars Beglinger reports financial support was provided by Innosuisse Swiss Innovation Agency. Lars Beglinger reports equipment, drugs, or supplies was provided by Levitronix GmbH. Daniel Steinert reports a relationship with Levitronix GmbH that includes: employment. Thomas Nussbaumer reports a relationship with Levitronix GmbH that includes: employment. If there are other authors, they declare that they have no known competing financial interests or personal relationships that could have appeared to influence the work reported in this paper.

Acknowledgments

This work is supported by the Swiss Innovation Agency Innosuisse project No. 46742.1. The authors gratefully thank Levitronix GmbH for their financial, scientific as well as technical contributions and acknowledge the Scientific Center for Optical and Electron Microscopy at ETH Zurich for their support and assistance.

Data availability

Data will be made available on request.

References

[1] B. Hallström, M. Lopez-Leiva, Description of a rotating ultrafiltration module, Desalination 24 (1) (1977) 273–279, http://dx.doi.org/10.1016/S0011-9164(00)88089-3.

[2] G. Belfort, J.M. Pimbley, A. Greiner, K.Y. Chung, Diagnosis of membrane fouling using a rotating annular filter. 1. Cell culture media, J. Membr. Sci. 77 (1) (1993) 1–22, http://dx.doi.org/10.1016/0376-7388(93)85231-K.

[3] G. Beaudoin, M.Y. Jaffrin, Plasma filtration in Couette flow membrane devices, Artif. Organs. 13 (1) (1989) 43–51, http://dx.doi.org/10.1111/j.1525-1594.1989.tb02831.x.

[4] G. Belfort, P. Mikulasek, J.M. Pimbley, K.Y. Chung, Diagnosis of membrane fouling using a rotating annular filter. 2. dilute particle suspensions of known particle size, J. Membr. Sci. 77 (1) (1993) 23–39, http://dx.doi.org/10.1016/0376-7388(93)85232-L.

[5] R.M. Lueptow, A. Docter, K. Min, Stability of axial flow in an annulus with a rotating inner cylinder, Phys. Fluids A 4 (11) (1992) 2446–2455, http://dx.doi.org/10.1063/1.858485.

[6] S.T. Wereley, R.M. Lueptow, Velocity field for Taylor–Couette flow with an axial flow, Phys. Fluids 11 (12) (1999) 3637–3649, http://dx.doi.org/10.1063/1.870228.

[7] A.C. Schlinker, K. Radwanski, C. Wegener, K. Min, W.M. Miller, Separation of in-vitro-derived megakaryocytes and platelets using spinning-membrane filtration, Biotechnol. Bioeng. 112 (4) (2015) 788–800, http://dx.doi.org/10.1002/bit.25477.

[8] L. Ibenana, R. Anderson, A. Gee, M. Gilbert, C. Cox, J.M. Hare, A. Brooks, L. Kelley, A. Khan, N. Lapteva, A. Orozco, D. Styers, D. Sumstad, I. Ugochi, D.H. McKenna, Assessment of the LOVO device for final harvest of novel cell therapies: a production assistance for cellular therapies multi-center study, Cytotherapy 24 (7) (2022) 691–698, http://dx.doi.org/10.1016/j.jcyt.2022.01.010.

[9] U. Hoffner, Dynamische Membranfiltration, CITplus 24 (1–2) (2021) 29–31, http://dx.doi.org/10.1002/citp.202100116.

[10] J.W. Chew, J. Kilduff, G. Belfort, The behavior of suspensions and macromolecular solutions in crossflow microfiltration: An update, J. Membr. Sci. 601 (2020) 117865, http://dx.doi.org/10.1016/j.memsci.2020.117865.

[11] A.L. Zydney, Continuous downstream processing for high value biological products: A review, Biotechnol. Bioeng. 113 (3) (2016) 465–475, http://dx.doi.org/10.1002/bit.25695.

[12] J. Walther, R. Godawat, C. Hwang, Y. Abe, A. Sinclair, K. Konstantinov, The business impact of an integrated continuous biomanufacturing platform for recombinant protein production, J. Biotech. 213 (2015) 3–12, http://dx.doi.org/10.1016/j.jbiotec.2015.05.010, Integrated Continuous Biomanufacturing: A New Paradigm for Biopharmaceutical Production.

[13] A.L. Zydney, Perspectives on integrated continuous bioprocessing—opportunities and challenges, Curr. Opin. Chem. Eng. 10 (2015) 8–13, http://dx.doi.org/10.1016/j.coche.2015.07.005.

[14] M.-F. Clincke, C. Mölleryd, Y. Zhang, E. Lindskog, K. Walsh, V. Chotteau, Very high density of CHO cells in perfusion by ATF or TFF in WAVE bioreactor™. Part I. Effect of the cell density on the process, Biotechnol. Prog. 29 (3) (2013) 754–767, http://dx.doi.org/10.1002/btpr.1704.

[15] J. Kim, C. Hu, C.M.E. Achkar, L.E. Black, J. Douville, A. Larson, M.K. Pendergast, S.F. Goldkind, E.A. Lee, A. Kuniholm, A. Soucy, J. Vaze, N.R. Belur, K. Fredriksen, I. Stojkovska, A. Tsytsykova, M. Armant, R.L. DiDonato, J. Choi, L. Cornelissen, L.M. Pereira, E.F. Augustine, C.A. Genetti, K. Dies, B. Barton, L. Williams, B.D. Goodlett, B.L. Riley, A. Pasternak, E.R. Berry, K.A. Pflock, S. Chu, C. Reed, K. Tyndall, P.B. Agrawal, A.H. Beggs, P.E. Grant, D.K. Urion, R.O. Snyder, S.E. Waisbren, A. Poduri, P.J. Park, A. Patterson, A. Biffi, J.R. Mazzulli, O. Bodamer, C.B. Berde, T.W. Yu, Patient-customized oligonucleotide therapy for a rare genetic disease, N. Engl. J. Med. 381 (17) (2019) 1644–1652, http://dx.doi.org/10.1056/NEJMoa1813279.

[16] H. Rogers, Investigational New Drug Application Submissions for Individualized Antisense Oligonucleotide Drug Products for Severely Debilitating or Life-Threatening Diseases: Clinical Recommendations; Draft Guidance for Sponsor-Investigators; Availability, Tech. Rep. FDA-2021-D-1140-0001, Food and Drug Administration, Silver Spring, MD, 2021.

[17] H. Tran, M. Moazami, H. Yang, D. McKenna-Yasek, C. Douthwright, C. Pinto, J. Metterville, M. Shin, N. Sanil, C. Dooley, A. Puri, A. Weiss, N. Wightman, H. Gray-Edwards, M. Marosfoi, R. King, T. Kenderdine, D. Fabris, R. Bowser, Brown Jr., Suppression of mutant C9orf72 expression by a potent mixed backbone antisense oligonucleotide, Nature Med. 28 (2022) http://dx.doi.org/10.1038/s41591-021-01557-6.

[18] S. Wang, S. Godfrey, J. Ravikrishnan, H. Lin, J. Vogel, J. Coffman, Shear contributions to cell culture performance and product recovery in ATF and TFF perfusion systems, J. Biotech. 246 (2017) 52–60, http://dx.doi.org/10.1016/j.jbiotec.2017.01.020.

[19] M. Gibson, Abbot, The use of modern centrifugal pumps in bioprocess design, in: Levitronix Bioprocessing Conference, Abbot, Cambridge, MA, USA, 2024, p. 2.

[20] R. Schöb, Centrifugal pump without bearings or seals, World Pumps 2002 (430) (2002) 34–37, http://dx.doi.org/10.1016/S0262-1762(02)80218-8.

[21] L. Beglinger, D. Steinert, T. Nussbaumer, J. Biela, Concept and design of a bearingless spinfilter, IEEE/ASME Trans. Mechatronics 28 (4) (2023) 1817–1825, http://dx.doi.org/10.1109/TMECH.2023.3274217.

[22] L. Beglinger, D. Zürcher, D. Steinert, T. Nussbaumer, J. Biela, Experimental evaluation of bearingless spinfilter topologies, Sep. Purif. Technol. 350 (2024) 127845, http://dx.doi.org/10.1016/j.seppur.2024.127845.

[23] S.S. Peppin, J.A. Elliott, Non-equilibrium thermodynamics of concentration polarization, Adv. Colloid Interface Sci. 92 (1) (2001) 1–72, http://dx.doi.org/10.1016/S0001-8686(00)00029-4.

[24] J.A. Brant, A.E. Childress, Assessing short-range membrane–colloid interactions using surface energetics, J. Membr. Sci. 203 (1) (2002) 257–273, http://dx.doi.org/10.1016/S0376-7388(02)00014-5.

[25] C. Duclos-Orsello, W. Li, C.-C. Ho, A three mechanism model to describe fouling of microfiltration membranes, J. Membr. Sci. 280 (1) (2006) 856–866, http://dx.doi.org/10.1016/j.memsci.2006.03.005.

[26] H. Ebner, Die kontinuierliche mikrofiltration von essig, Chem. Ing. Tech. 53 (1) (1981) 25–31, http://dx.doi.org/10.1002/cite.330530104.

[27] M.T. Nguyen, Deckschichtbildung in Kapillarmembranen bei der Querstrom-Mikrofiltration und Ihre Beeinflussung Durch Polymere Flockungsmittel (Ph.D. thesis), TU Dresden, 2004.

[28] S. Kuiper, C. van Rijn, W. Nijdam, G. Krijnen, M. Elwenspoek, Determination of particle-release conditions in microfiltration: a simple single-particle model tested on a model membrane, J. Membr. Sci. 180 (1) (2000) 15–28, http://dx.doi.org/10.1016/S0376-7388(00)00430-0.

[29] G.I. Taylor, Stability of a viscous liquid contained between two rotating cylinders, Philos. Trans. R. Soc. Lond. Ser. A Math. Phys. Eng. Sci. 223 (1923) 289–343.

[30] F. Menter, Zonal two equation k-w turbulence models for aerodynamic flows, in: AIAA 23rd Fluid Dynamics, Plasmadynamics, and Lasers Conference, 1993, 1993.

[31] C. Hewitt, A. Nienow, The scale-up of microbial batch and fed-batch fermentation processes, Adv. Appl. Microbiol. 62 (2007) 105–135, http://dx.doi.org/10.1016/S0065-2164(07)62005-X.

[32] M.Y. Jaffrin, L.-H. Ding, O. Akoum, A. Brou, A hydrodynamic comparison between rotating disk and vibratory dynamic filtration systems, J. Membr. Sci. 242 (1–2) (2004) 155–167, http://dx.doi.org/10.1016/j.memsci.2003.07.029.

[33] T. Tanzeglock, M. Soos, G. Stephanopoulos, M. Morbidelli, Induction of mammalian cell death by simple shear and extensional flows, Biotechnol. Bioeng. 104 (2) (2009) 360–370, http://dx.doi.org/10.1002/bit.22405.

[34] R. Godoy-Silva, J.J. Chalmers, S.A. Casnocha, L.A. Bass, N. Ma, Physiological responses of CHO cells to repetitive hydrodynamic stress, Biotechnol. Bioeng. 103 (6) (2009) 1103–1117, http://dx.doi.org/10.1002/bit.22339.

[35] J. Varley, J. Birch, Reactor design for large scale suspension animal cell culture, Cytotechnology 29 (3) (1999) 177–205, http://dx.doi.org/10.1023/A:1008008021481.

[36] N. Hutchinson, N. Bingham, N. Murrell, S. Farid, M. Hoare, Shear stress analysis of mammalian cell suspensions for prediction of industrial centrifugation and its verification, Biotechnol. Bioeng. 95 (3) (2006) 483–491, http://dx.doi.org/10.1002/bit.21029.

[37] M. Mollet, R. Godoy-Silva, C. Berdugo, J.J. Chalmers, Computer simulations of the energy dissipation rate in a fluorescence-activated cell sorter: Implications to cells, Biotechnol. Bioeng. 100 (2) (2008) 260–272, http://dx.doi.org/10.1002/bit.21762.

[38] B. Vickroy, K. Lorenz, W. Kelly, Modeling shear damage to suspended CHO cells during cross-flow filtration, Biotechnol. Prog. 23 (1) (2007) 194–199, http://dx.doi.org/10.1021/bp060183e.

[39] M. Mollet, R. Godoy-Silva, C. Berdugo, J.J. Chalmers, Acute hydrodynamic forces and apoptosis: A complex question, Biotechnol. Bioeng. 98 (4) (2007) 772–788, http://dx.doi.org/10.1002/bit.21476.

[40] W. Hu, R. Gladue, J. Hansen, C. Wojnar, J.J. Chalmers, The sensitivity of the dinoflagellate crypthecodinium cohnii to transient hydrodynamic forces and cell-bubble interactions, Biotechnol. Prog. 23 (6) (2007) 1355–1362, http://dx.doi.org/10.1021/bp070306a.

[41] L. Rosenhead, Laminar Boundary Layers: An Account of the Development, Structure, and Stability of Laminar Boundary Layers in Incompressible Fluids, Together with a Description of the Associated Experimental Techniques, in: Fluid Motion Memoirs, Clarendon Press, 1963.

[42] P.R. Childs, Chapter 6 - rotating cylinders, annuli, and spheres, in: P.R. Childs (Ed.), Rotating Flow, Butterworth-Heinemann, Oxford, 2011, pp. 177–247, http://dx.doi.org/10.1016/B978-0-12-382098-3.00006-8.

[43] P. Püntener, Haemolysis in Bearingless Centrifugal Pumps (Ph.D. thesis), ETH Zurich, 2020.